Available online at www.sciencedirect.com
ScienceDirect
Journal of Power Sources 165 (2007) 196–209
JOURNAL OF POWER SOURCES
www.elsevier.com/locate/jpowsour

# Unsteady 2D PEM fuel cell modeling for a stack emphasizing thermal effects

Yuyao Shan [a,*], Song-Yul Choe [a], Seo-Ho Choi [b]

[a] *Department of Mechanical Engineering, Auburn University, Auburn, United States*
[b] *Fuel Cell Vehicle Team, Hyundai Motor Company & Kia Motors Corporation, United States*

Received 28 September 2006; received in revised form 3 December 2006; accepted 5 December 2006
Available online 20 December 2006

**Abstract**

Models currently used for analyses of thermal and water behavior of a PEM fuel cell are based 3D computational fluid dynamics (CFD). However, the analyses are limited to a single cell with static behavior. Thus, these models cannot be used for analyses of dynamic behavior of a stack that continuously varies according to operating conditions. The model proposed describes dynamic behavior of a stack with two adjoining cells and endplate assembly, and work as a current controlled voltage source that can be used for optimization of BOPs and the associated controls. Simulations have been conducted to analyze start-up behaviors and the performance of the stack. Our analyses deliver following results: (1) dynamic temperature distribution in both the through-plane direction and the along channel direction of the fuel cell stack, (2) effects influencing the source terms of current density, and (3) dynamic oxygen concentration distribution. The temperature profile and its variation propensity are comparable to the previous results [Y. Shan, S.Y. Choe, J. Power Sources, 145 (1) (2005) 30–39; Y. Shan, S.Y. Choe, J. Power Sources, in press].


*Keywords:* PEMFC; Stack; Dynamics; Temperature distribution

## 1. Introduction

Current computational models available in both the academic world and the market are either too simple or complex to particularly describe dynamic behaviors of a PEM fuel cell stack. Some authors [1–3] simply employ empirical equations, whose coefficients are obtained by fitting a polarization curve. This approach is useful for a design of the power system, but ignores effects of temperature, water and reactants on the cell performances. Thus, it can hardly describe the complex behaviors of a stack. In addition, 2D or 3D models using CFD techniques proposed by other authors [4–7] can capture the complexity of a single cell, but are limited to steady state analyses and unable to represent an unsteady behavior of a stack. Um et al. [8] published a 2D CFD model that describes the transient behavior of the bulk flow, species and electro-chemical reactions in a single cell, which has been extended to an isothermal 3D model [10,11]. Likewise, Dutta et al. [9] developed a 3D model with an isothermal flow in a cell that embeds a serpentine-type gas channel. However, the simulation is conveyed by the use of commercial software package, Fluent, and they studied both the gas distribution and water generation in a single cell. Um and Wang [10] developed a 3D CFD model for a single cell. They intensively studied species and water removal in a straight and an inter-digitated flow channel and found enhancement of the performance at the inter-digitated shape. Furthermore, Wang and Wang [11] simulated a single cell with 36 gas serpentine channels taking a low humidity condition by using the software package of Star-CD and presented the mechanism of the species transport and the associated current density distribution. Unlike the studies above, Ju et al. [12] considered a non-isothermal condition in the 3D plane and simulated a cell with a straight channel by using Star-CD.

All of works above, however, have been focused on description of a single cell and are still unable to describe a stack and time-varying behaviors. On the other hand, the dynamic behavior of a stack can be improved by adding a simplified thermodynamic model, which is proposed by Sundaresan [13,14]. The model regards a cell as a composition of layers and is used to analyze the start-up behavior from a sub-freezing temperature. However, the model does not fully consider several factors:

* Corresponding author. Tel.: +1 3342206533; fax: +1 3348443307.
*E-mail address:* shanyuy@auburn.edu (Y. Shan).

0378-7753/$ – see front matter © 2006 Elsevier B.V. All rights reserved.
doi:10.1016/j.jpowsour.2006.12.022

**Nomenclature**

| | |
|---|---|
| $b$ | membrane extension coefficient ($m^2\ m^{-3}$) |
| $c$ | mole concentration ($mol\ m^{-3}$) |
| $C_p$ | thermal capacity ($J\ mol^{-1}\ K^{-1}$) |
| $D$ | diffusion coefficient ($m^2\ s^{-1}$) |
| $F$ | Faraday number ($C\ mol^{-1}$) |
| $I$ | current density ($A\ m^{-2}$) |
| $j$ | current density ($A\ m^{-3}$) |
| $J$ | mass flow rate ($kg\ m^{-2}$) |
| $k$ | thermal conductivity ($W\ m^{-1}\ K^{-1}$) |
| $K$ | gas permeability ($m^2$) |
| $L$ | length (m) |
| $M$ | mole mass ($kg\ mol^{-1}$) |
| $n$ | electro-osmotic coefficient |
| $R$ | universal gas constant ($J\ mol^{-1}\ K^{-1}$) |
| $S$ | source term |
| $T$ | temperature (K) |
| $u$ | velocity ($m\ s^{-1}$) |
| $V$ | voltage (V) |
| $X$ | dimensionless mol concentration ($m^{-3}$) |

*Greek letters*

| | |
|---|---|
| $\alpha$ | transfer coefficient |
| $\gamma$ | water transfer coefficient ($m\ s^{-1}$) |
| $\varepsilon$ | porosity |
| $\eta$ | over-potential (V) |
| $\lambda$ | water content |
| $\mu$ | viscosity ($kg\ m^{-1}\ s^{-1}$) |
| $\rho$ | density ($kg\ m^{-3}$) |
| $\sigma$ | conductivity ($s\ m^{-1}$) |
| $\Phi$ | potential (V) |

*Subscripts*

| | |
|---|---|
| a | anode |
| c | cathode |
| e | electrolyte |
| OC | open circuit |
| s | solid matrix |
| tota | anode total |
| totc | cathode total |

*Superscripts*

| | |
|---|---|
| eff | effective |
| ref | reference value |

(1) flow rate of species at the inlet of the channel must be the same as that at the outlet of the channel. Thus, no fluid dynamics are considered; (2) heat source terms in both the catalysts are empirically calculated with values suggested by the Wohr and Peinecke's model [15]. Accordingly, the anode source term is presumed as a relatively large value that in fact should be referred to be around zero [16]. As a result, the model does not show asymmetric phenomena of performance through the stack. Wetton et al. [17] proposed an explicit stack thermal model with the coolant channel coupled with a 1D cell model [18]. It shows a great temperature gradient of the stack, but with no dynamics at all. We proposed an enhanced quasi 1D stack model [19,20] based on the previous single cell model that considers the thermal and fluid dynamics. As a result, the model proposed is capable of capturing the dynamic temperature distribution including the asymmetrical effects in the stack, but missing the water distribution that are improved by adding an empirical relationship between the flooding effect and the current density and temperature.

As the matter of fact, none of current models can fully describe the stack behavior. On the system aspects, the model should be a current controlled voltage source, so that the load can be easily integrated into a stack model. Moreover, the domain should be so set up that can integrate two endplates and bus plate at the anodic and cathode side with an interface plate that embeds a coolant channel as well as two bipolar plates with the repeating basic cell unit.

In fact, the mass and charge transport as well as the heat flux in the basic cell unit is described by the use of the Navier–Stokes and the potential and energy conservation equation. Likewise, the heat flux in the coolant channel is described by using both the Navier–Stokes and the energy conservation equations, while the rest of plate regions are described by the heat conservation equations. The partial differential equations (PDEs) are solved by the SIMPLE [21] algorithm. In the following sections, details on the 2D models are summarized, which includes assumptions, simulation set-up and equations used for a description of the model proposed. Included are the procedure to solve the equations and a generation of grids. At the end, simulations are conveyed with boundary conditions used for the individual domain and the results are discussed.

## 2. Model description

### 2.1. Modeling domain and assumptions

Major assumptions are made for a 2D stack model as follows:

1. Reactants as ideal gases;
2. Incompressible and laminar flow;
3. Isotropic and homogeneous electrodes, catalyst layers and membrane;
4. Identical inlet conditions of each cell for both the cathode and anode as well as coolant channel;
5. Constant thermal conductivity of the materials in a fuel cell;
6. Neglect diffusions caused by multi-component;
7. No contact resistance;
8. No liquid water generated;
9. The source/sink term can be neglected in a PEFC where electrochemical reactions occur [26].

In addition, it is assumed that a single cell has a structure of sandwiched layers shown in Fig. 1. The anode sides of the cells are located on the left hand side, while the cathode sides on the right hand side. The single cell domain for the model is constructed with seven different layers that are symmetrically placed at the membrane layer. A gas flow channel, a gas diffusion

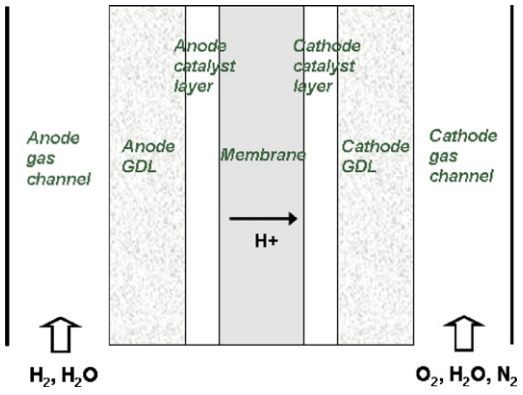


Fig. 1. Single cell schematic configuration [8].

layer and a catalyst layer for the anode side are located at the left side of the membrane layer as well as those for cathode side with a reversed order. Thus, a stack can be easily constructed by repeating this basic unit domain and adding bipolar plates with coolant channel, interface and bus plates, and end plates shown in Fig. 2.

Finally, a stack model is completed by coupling of the domains for the basic units with two endplate assemble. Finally, simulation can be performed.

### 2.2. Model description

#### 2.2.1. Charge transport

Protons and electrons are the positively and negatively charged ions. The proton transfer in the proton conducting regions and the electron transfer in the electronic conducting regions determines the potential distribution in a cell. The polymer as electrolyte in the membrane and the catalysts belongs to the proton conducting region, while the catalysts, GDLs and BPs including gas flow and coolant channels are regarded as electrode, which is repeating in the stack configuration.

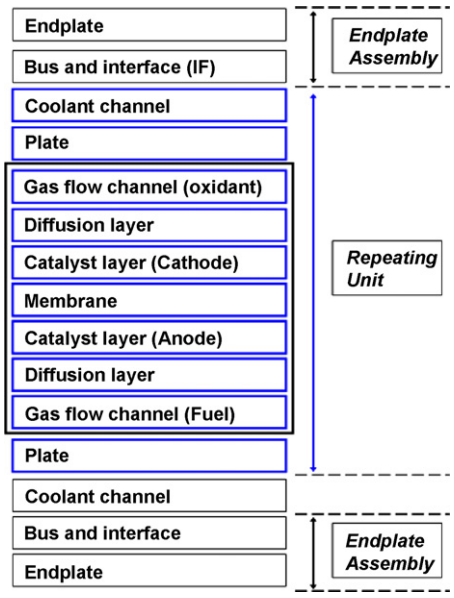


Fig. 2. Stack schematic configuration.

The potentials in the electrolyte are governed by the potential conservation equation according to the Ohm's law:

$$\nabla(\sigma_e \nabla \Phi_e) + S_\Phi = 0 \quad (1)$$

$$S_\Phi = j \text{ in the two catalyst layers} \quad (1a)$$

$$S_\Phi = 0 \text{ in the membrane layer} \quad (1b)$$

where the proton conductivity $\sigma_e$ is a function of temperature and the water content in the polymer material [24];

$$\sigma_e = 100 \exp\left(1268\left(\frac{1}{303} - \frac{1}{T}\right)\right) \times (0.005139\lambda_{H_2O/SO_3} - 0.00326) \quad (2)$$

According to the Butler–Volmer equation [1,8], the current densities in the anode and cathode catalysts can be expressed by the exchange current density, reactant concentration, temperature and over-potentials according to the Butler–Volmer Eqs. (3) and (4):

$$j_a = a j_{0,a}^{ref}\left(\frac{X_{H_2}}{X_{H_2,ref}}\right)^{1/2}\left(\frac{\alpha_a + \alpha_c}{RT} F\eta\right) \quad (3)$$

$$j_c = -a j_{0,c}^{ref}\left(\frac{X_{O_2}}{X_{O_2,ref}}\right)^{1/2} \exp\left(-\frac{\alpha_c F}{RT}\eta\right) \quad (4)$$

where the surface over-potential is defined as a difference between the electrodes and electrolyte referring to an equilibrium state.

$$\eta(x, y) = V - V_{equlibrium} = \Phi_s - \Phi_e - V_{OC} \quad (5)$$

where $\Phi_s$ and $\Phi_e$ are the potentials of the electrons conducting solid materials and electrolyte, respectively, at electrodes and electrolyte interface. The open circuit potential at the anode is assumed to be zero, while the open circuit potential at the cathode becomes a function of a temperature as [1,9]:

$$V_{OC}^c = 0.0025T + 0.2329 \quad (6)$$

Then, the local current density for the protons can be simplified with

$$I = -\sigma_e \nabla \Phi_e \quad (7)$$

On the other hand, the electronic conducting region includes the entire stack except the membranes and the two endplates. In fact, the electronic conductivity in the entire electron conducting layers is at least two orders higher than the proton conductivity. Thus, the potential drop caused by the electrons transfer is negligible. Therefore, the values of the potentials in the electron conducting regions can be regarded as a single value. When the load current is applied to the model as an input, the voltage drops in the electron conducting regions vary because of the flow field being changed. This effect is reflected by using a current conservation equation at an equilibrium state of the potential field and described by the following equations:

$$f(\Phi_e') = \int_V j_a' \, dV - I_{input} L_{ch} = 0 \text{ in anode catalyst layers} \quad (8)$$

$$f(\Phi_s') = \int_V j_c' \, dV - I_{input} L_{ch} = 0 \text{ in cathode catalyst layers} \quad (9)$$

Accordingly, both of the electrolyte potential distribution and electrode potential ($\Phi_s$ and $\Phi_m$) can be corrected. The resulting equations are implicit and can be solved numerically.

$$F(\Phi_e + \Delta\Phi_e) = \int_V j_{a,(\Phi_e+\Delta\Phi_e)} \, dV - I_{input} L_{ch} = 0 \quad (10)$$

$$F(\Phi_s + \Delta\Phi_s) = \int_V j_{c,(\Phi_s+\Delta\Phi_s)} \, dV - I_{input} L_{ch} = 0 \quad (11)$$

Then, the new electrolyte potential is obtained by adding the correction factor calculated in the anode catalyst layer to the previous value of the potential for the domain of the catalyst and the membrane, while the previous of the potentials are obtained by solving the potential conservation equation (Eq. (1)). Likewise, the new electrode potentials are calculated by adding the correction factor calculated in the cathode catalyst layer to the previous value of the potential.

$$\Phi_e^{new} = \Phi_e^{old} + \Delta\Phi_e, \ \Phi_s^{new} = \Phi_s^{old} + \Delta\Phi_s \quad (12)$$

*2.2.2. Mass transport*

*2.2.2.1. Anode/cathode side.* The anode side includes a gas channel, a gas diffusion layer, and catalysts. Like the anodic side, the cathode side includes a cathode gas channel, a gas diffusion layer and a catalyst. The role of the layers is to provide a pathway for the transfer of the fuel and humidity from the inlet to the catalysts. The flow field can be a shape of either serpentine or inter-digitated channels. Compared to the serpentine shape, the inter-digitated type can dramatically increase the mass transfer in the gas diffusion layer by convection. In this study, a straight channel is selected to represent a serpentine channel. Then, the mass transport in the channel is governed by the following equations:

- Mass conservation

$$\frac{\partial(\rho\varepsilon)}{\partial t} + \nabla(\rho\varepsilon\vec{u}) = 0 \quad (13)$$

- Momentum conservation

$$\frac{\partial(\rho\varepsilon\vec{u})}{\partial t} + \nabla(\rho\varepsilon\vec{u}\vec{u}) = -\varepsilon\nabla p + \nabla(\varepsilon\mu^{eff}\nabla\vec{u}) + S_u \quad (14)$$

$$S_u = -\frac{\mu}{K}\vec{u} \quad \text{in the gas diffusion and catalyst layers [5]} \quad (14a)$$

$$S_u = 0 \quad \text{in the gas channel} \quad (14b)$$

Similarly, the hydrogen concentration can be obtained by using the species conservation equation:

$$\frac{\partial(\varepsilon X_{H_2})}{\partial t} + \nabla(\varepsilon\vec{u}X_{H_2}) = \nabla(D_{H_2}^{eff}\nabla X_{H_2}) + S_{H_2} \quad (15)$$

$$S_{H_2} = -\frac{j_a}{2Fc_{tota}} \quad \text{in gas diffusion layers and catalyst layers [1]} \quad (15a)$$

$$S_{H_2} = 0 \quad \text{in gas channel} \quad (15b)$$

where the effective diffusivity $D_{H_2}^{eff}$ is,

$$D_{H_2}^{eff} = \varepsilon^{1.5} D_{H_2}, \qquad X_{O_2} = \frac{c_{H_2}}{c_{tota}} \quad (16)$$

and the species conservation equations for cathode are:

$$\frac{\partial(\varepsilon X_{O_2})}{\partial t} + \nabla(\varepsilon\vec{u}X_{O_2}) = \nabla(D_{O_2}^{eff}\nabla X_{O_2}) + S_{O_2} \quad (17)$$

$$S_{O_2} = \frac{j_c}{4Fc_{totc}} \quad \text{in catalyst layers} \quad (17a)$$

$$S_{O_2} = 0 \quad \text{in gas channel and gas diffusion layers} \quad (17b)$$

$$\frac{\partial(\varepsilon X_{H_2O})}{\partial t} + \nabla(\varepsilon\vec{u}X_{H_2O}) = \nabla(D_{H_2O}^{eff}\nabla X_{H_2O}) + S_{H_2O} \quad (18)$$

$$S_{H_2O} = -\frac{j_c}{2Fc_{totc}} \quad \text{in catalyst layers} \quad (18a)$$

$$S_{H_2O} = 0 \quad \text{in gas channel and gas diffusion layers} \quad (18b)$$

where the effective diffusivities and mole fractions of the oxygen and water are as follows:

$$D_{O_2}^{eff} = \varepsilon^{1.5} D_{O_2}, \qquad D_{H_2O}^{eff} = \varepsilon^{1.5} D_{H_2O}, \qquad X_{O_2} = \frac{c_{O_2}}{c_{totc}},$$
$$X_{H_2O} = \frac{c_{H_2O}}{c_{totc}} \quad (19)$$

*2.2.2.2. Water transport in membrane.* Water distribution in the membrane is determined by the electro-osmotic force, the diffusion and convection. At a single phase, the influence of the convection is negligible and the water concentration can be described by the following equations:

$$\frac{\partial c_e^{H_2O}}{\partial t} = \nabla(D_e^{H_2O}\nabla c_e^{H_2O}) - \nabla\left(n_d\frac{I}{F}\right) \quad (20)$$

The first term describes the diffusion dependent water flux and the second one does the water transport dependent upon the electro-osmotic force. And the electro-osmotic coefficient is a function of the local water content ($n_d$):

$$n_d = 2.5\frac{\lambda_{H_2O/SO_3}}{22} \quad (21)$$

The water content $\lambda_{H_2O/SO_3}$ is a function of the water uptake obtained from the water concentration:

$$\lambda_{H_2O/SO_3} = \frac{c_e^{H_2O}}{\rho_{dry}^e/M^e - bc_e^{H_2O}} \quad (22)$$

The water flux at the boundary interfaces between the catalysts and membrane is described by using the Robin type boundary condition, which presents the relationship between

the water concentration in the gas phase and in the membrane [25].

$$J_{bc}^{H_2O} = \gamma(c_e^{H_2O} - c_{e,eq}^{H_2O}) - \frac{n_d}{F} I \tag{23}$$

However, compared to the reactants transport phenomena in the gas diffusion layer, the water transport in the membrane is more complicated. Some experiments showed the different time scales of the hydration and dehydration processes in the Nafion [25]. It takes about tens of seconds for liquid water to get adsorbed, which is two orders of magnitude larger than for the dehydration process. This hydration–dehydration dichotomy might result from two reasons: (1) the water diffusion coefficient in the membrane is a function of local water concentration. And it varies with the changing of water concentration; (2) the Robin type water transfer coefficient $\gamma$ is also affected by the water concentration at the boundaries between the membrane and catalysts.

Springer et al. [23] proposed a coefficient of water diffusion equation that is derived from experimental results:

$$D_e^{H_2O} = D' \exp\left(2416\left(\frac{1}{303} - \frac{1}{T_e}\right)\right) \tag{24}$$

where

$$D' = \begin{cases} 2.64227\text{E} - 13\lambda_{H_2O/SO_3} & 1.23 > \lambda_{H_2O/SO_3} \\ 7.75\text{E} - 11\lambda_{H_2O/SO_3} - 9.5\text{E} - 11 & 6 \geq \lambda_{H_2O/SO_3} \geq 1.23 \\ 2.5625\text{E} - 11\lambda_{H_2O/SO_3} - 2.1625\text{E} - 10 & 14 > \lambda_{H_2O/SO_3} > 6 \end{cases} \tag{24a}$$

According to the data proposed Berg [7], the Robin type water transfer coefficient is chosen with $\gamma_l = 5 \times 10^{-4}$ when a membrane is fully immersed into liquid water, while $\gamma_g = 4.5 \times 10^{-6}$ for the membrane dried in a gaseous condition.

*2.2.2.3. Coolant flows.* The coolant flow channels embedded in bipolar plates or endplates provide part of the pathway for the coolant circuits. After the heat exchange between the coolants and the heat source has occurred at the wall, the coolant releases most of the heat to the environment via the radiator. If the coolant flow channel is assumed as a straight channel, the flow of the coolant can be governed by the following equations:

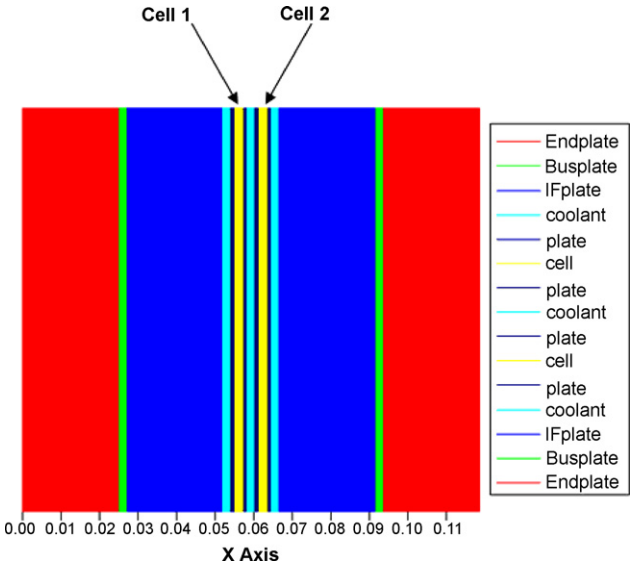


Fig. 3. Stack geometry information.

- Mass conservation

$$\frac{\partial \rho}{\partial t} + \nabla(\rho \vec{u}) = 0 \tag{25}$$

Table 1
Parameters for 2D models

| Quantity | Value |
|---|---|
| Gas channel length, $L$ (cm) | 7.112 |
| Oxygen diffusivity in gas ($cm^2\ s^{-1}$) | $5.2197 \times 10^{-2}$ |
| Hydrogen diffusivity in gas ($cm^2\ s^{-1}$) | $2.63 \times 10^{-2}$ |
| Dissolved oxygen diffusivity in active layer and membrane ($cm^2\ s^{-1}$) | $2.0 \times 10^{-4}$ |
| Dissolved hydrogen diffusivity in active layer and membrane ($cm^2\ s^{-1}$) | $2.59 \times 10^{-6}$ |
| Faraday constant, $F$ ($C\ mol^{-1}$) | 96,487 |
| Permeability of backing layer, $K$ ($cm^2$) | $1.76 \times 10^{-6}$ |
| Universal gas constant, $R$ ($J\ mol^{-1}\ K^{-1}$) | 8.314 |
| Cathodic transfer coefficient | 2 |
| Anodic transfer coefficient | 2 |
| Inlet nitrogen-oxygen mole fraction | 0.79/0.21 |
| Air-side inlet pressure/fuel-side inlet pressure (atm) | 5/3 |
| $O_2$ stoichiometric flow ratio | 3.0 |
| $H_2$ stoichiometric flow ratio | 2.8 |
| Reference exchange current density $x$ area of anode ($A\ cm^{-3}$) | $5.0 \times 10^2$ |
| Reference exchange current density $x$ area of cathode ($A\ cm^{-3}$) | $1.0 \times 10^{-4}$ |
| Total mole concentration at the anode side ($mol\ cm^{-3}$) | $66.81 \times 10^{-6}$ |
| Total mole concentration at the cathode side ($mol\ cm^{-3}$) | $17.81 \times 10^{-6}$ |

Table 2
Geometry parameters for the fuel cell

| | Thickness, $m$ | Heat conductivity ($W\,m^{-1}\,K^{-1}$) | Heat capacity ($J\,kg^{-1}\,K^{-1}$) | Density ($kg\,m^{-3}$) |
|---|---|---|---|---|
| GDL | 0.0004 | 4 | 840 | 2000 |
| Catalyst layer | 0.000065 | 0.2 | 770 | 387 |
| Membrane layer | 0.000183 | 0.21 | 1100 | 1967 |
| Gas channel | 0.001 | 52 | 935 | 1400 |
| Plate | 0.001 | 52 | 935 | 1400 |
| Coolant channel | 0.001 | 30 | 935 | 1400 |

| | |
|---|---|
| GDL porosity | 0.4 |
| Catalyst layer porosity | 0.2 |
| GDL tortuosity | 3.725 |
| Bipolar plate contact area percentage | 0.5 |
| Membrane molecular mass ($kg\,mol^{-1}$) | 1.1 |
| Fuel cell area ($m^2$) | 0.0367 |
| Fuel cell active area ($m^2$) | 0.03 |

- Momentum conservation

$$\frac{\partial(\rho\vec{u})}{\partial t} + \nabla(\rho\vec{u}\vec{u}) = -\nabla p + \nabla(\mu\nabla\vec{u}) \tag{26}$$

*2.2.3. Heat flux in a stack*

The heat in the stack is produced by five different sources that include the entropy and losses caused by over-potentials at two catalysts, proton conductivity, electron conductivity, and the phase change of water. Under the condition of a single phase, there is no heat generation associated with the phase change. In addition, all the heat generated is then transferred from the source to the fluid by conduction and convection and completely removed out of the stack by the coolant and gases at the channel outlet. Then, the thermal behavior of a stack can be governed by the energy conservation equation [5]:

$$\frac{\partial}{\partial t}(\rho_{\mathrm{m}} C_{\mathrm{p,m}} T) + \vec{\nabla}(\varepsilon\rho_{\mathrm{f}}\vec{u} C_{\mathrm{p,f}} T) = \vec{\nabla}(k^{\mathrm{eff}}\vec{\nabla}T) + S_T \tag{27}$$

$$S_T = j\left(\eta + T\frac{\mathrm{d}V_{\mathrm{OC}}}{\mathrm{d}T}\right) + \frac{I^2}{\sigma_{\mathrm{e}}} \quad \text{in the catalyst layers} \tag{27a}$$

$$S_T = \frac{I^2}{\sigma_{\mathrm{e}}} \quad \text{in the membrane layer} \tag{27b}$$

$$S_T = 0 \quad \text{in the gas channel and gas diffusion layers} \tag{27c}$$

where the overall density and thermal conductivity are defined as

$$\rho_{\mathrm{m}} = \rho_{\mathrm{f}} + \rho_{\mathrm{stack}}, \qquad k^{\mathrm{eff}} = k_{\mathrm{f}}^{\mathrm{eff}} + k_{\mathrm{stack}}^{\mathrm{eff}} \tag{28}$$

and the fluid mixture properties are

$$\rho_{\mathrm{f}} = \sum_i \rho_i X_i, \qquad \rho_{\mathrm{f}} C_{\mathrm{p,f}} = \sum_i \rho_i C_{\mathrm{p},i} \tag{29}$$

*2.2.4. Boundary conditions*

*2.2.4.1. For the fluid flow.* The fluid velocities at the inlet of the anode, the cathode, and the coolant channel are predetermined. The standard exit boundary and no-slip boundary conditions are applied to the channel exits and walls, respectively. In the species field, the inlet species concentrations are given, while the species gradients at the channel exits and walls are set to zero. All boundary conditions for the fluid flow are summarized as below.

Table 3
Initial values

| Quantity | Value |
|---|---|
| Temperature (K) | 353 |
| Oxygen nondimensinal concentration | 0.21 |
| Cathode inlet velocity ($m\,s^{-1}$) | 0.334 |
| Anode inlet velocity ($m\,s^{-1}$) | 0.157 |

At the anode inlet (30) and outlet (31)

$$u = 0, \quad v = v_{\mathrm{H_2,in}}, \quad X_{\mathrm{H_2}} = X_{\mathrm{H_2,in}}, \quad T_{\mathrm{H_2}} = T_{\mathrm{H_2,in}} \tag{30}$$

$$u = 0, \quad \frac{\partial v}{\partial y} = 0, \quad \frac{\partial X_{\mathrm{H_2O}}}{\partial y} = 0, \quad \frac{\partial X_{\mathrm{H_2}}}{\partial y} = 0, \quad \frac{\partial T_{\mathrm{H_2}}}{\partial y} = 0 \tag{31}$$

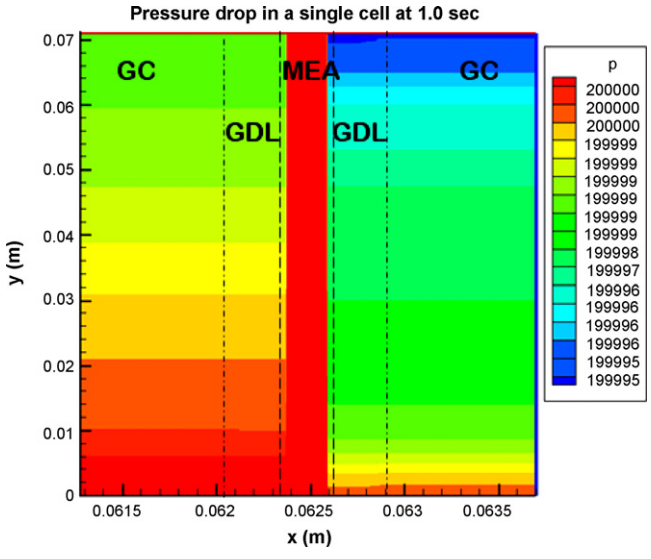


Fig. 4. Pressure drop in the cell 1 (Unit: Pa).

At the cathode inlet (32) and outlet (33)

$$u = 0, \quad v = v_{O_2}, \quad X_{O_2} = X_{O_2,\text{in}}, \quad T_{\text{air}} = T_{\text{air,in}} \tag{32}$$

$$u = 0, \quad \frac{\partial v}{\partial y} = 0, \quad \frac{\partial X_{H_2O}}{\partial y} = 0, \quad \frac{\partial X_{O_2}}{\partial y} = 0, \quad \frac{\partial T_{\text{air}}}{\partial y} = 0 \tag{33}$$

At the coolant inlet (34) and outlet (35)

$$u = 0, \quad v = v_{\text{Coolant,in}}, \quad T_{\text{Coolant}} = T_{\text{Coolant,in}} \tag{34}$$

$$u = 0, \quad \frac{\partial v}{\partial y} = 0, \quad \frac{\partial T_{\text{coolant}}}{\partial y} = 0 \tag{35}$$

At the wall

$$u = 0, \quad v = 0, \quad \frac{\partial X_{H_2}}{\partial y} = 0, \quad \frac{\partial X_{O_2}}{\partial y} = 0, \quad \frac{\partial X_{H_2O}}{\partial y} = 0 \tag{36}$$

*2.2.4.2. For the electrolyte potential field.* The boundary conditions for the gradient of the electrolyte potential field are set to zero at the left anode catalyst as well as the right cathode catalysts

$$\frac{\partial \Phi_e}{\partial x} = 0 \tag{37}$$

*2.2.4.3. For the electrolyte potential field.* The boundary conditions for the gradient of the electrical potential field is set as zeros at the right anode catalyst boundary as well as the left cathode catalyst boundary

$$\frac{\partial \Phi_s}{\partial x} = 0 \tag{38}$$

## 3. Numerical solution

First of all, the conservation equations are discretized by using the control-volume-based finite difference method. The flow solution procedure is based upon the SIMPLE algorithm [21] with a collocated grid cell centered approach.

The simulation set-up for the stack includes two endplate assemblies, two coolant and flow channels, and two cells with one bipolar plate (Fig. 3).

The input parameters used for the current simulation are summarized (see Tables 1–3).

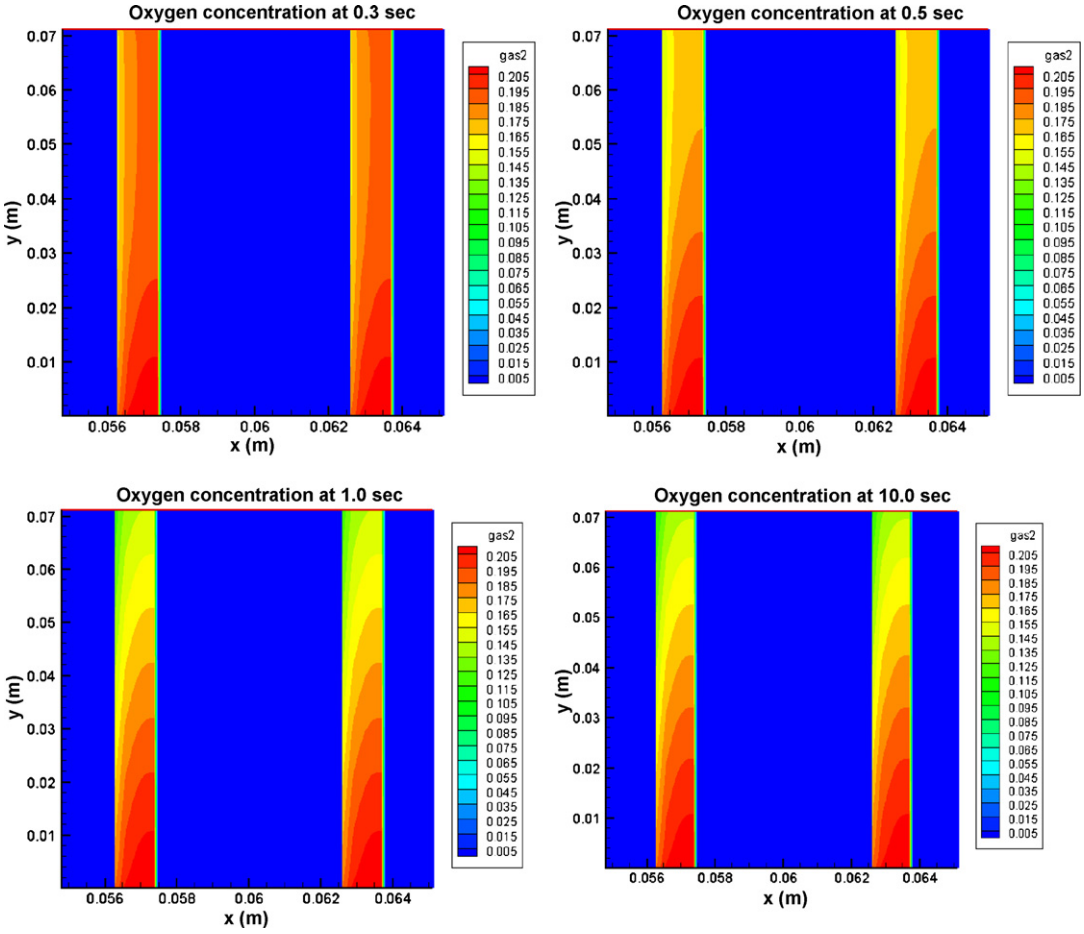


Fig. 5. Dynamics of oxygen concentration at two cells.

## 4. Analyses

Fig. 4 shows the simulated result of the pressure field in the cell number 1. The pressure drop on the anode flow channel is very small and negligible, simply because the viscosity of the hydrogen is smaller than that of the air on the cathode. In addition, the velocity of the anode gas is slower than that of the cathode one. It is noted that the Reynolds number for the cathode is 23.7 for the simulation and the resulting pressure drop is 10 Pa approximately, which is comparable to the results in Ref. [22].

Fig. 5 shows transient behaviors of the oxygen concentrations in the cathode side flow channels. When the simulation starts, the oxygen concentrations are changing, but still identical in the both channels because the temperature effects on the reaction is not so high and the reactants consumed are not so different in the two cells. However, the concentration on the left side is lower than the right side in the channel because of the oxygen being consumed by the chemical reactions. The steady state has been reached after the 1 s.

Fig. 6 shows a transient behavior of the source term of the current density generated in the cathode catalysts of the cell 1 at the 0.3, 0.5, 1 and 10 s. The magnitude of the current density largely varies in the 1 s. In fact, the source term of the current density are generally influenced by three phenomena with the rise of the temperature, the distribution of the cathode overpotentials and the concentration of the reactants. The

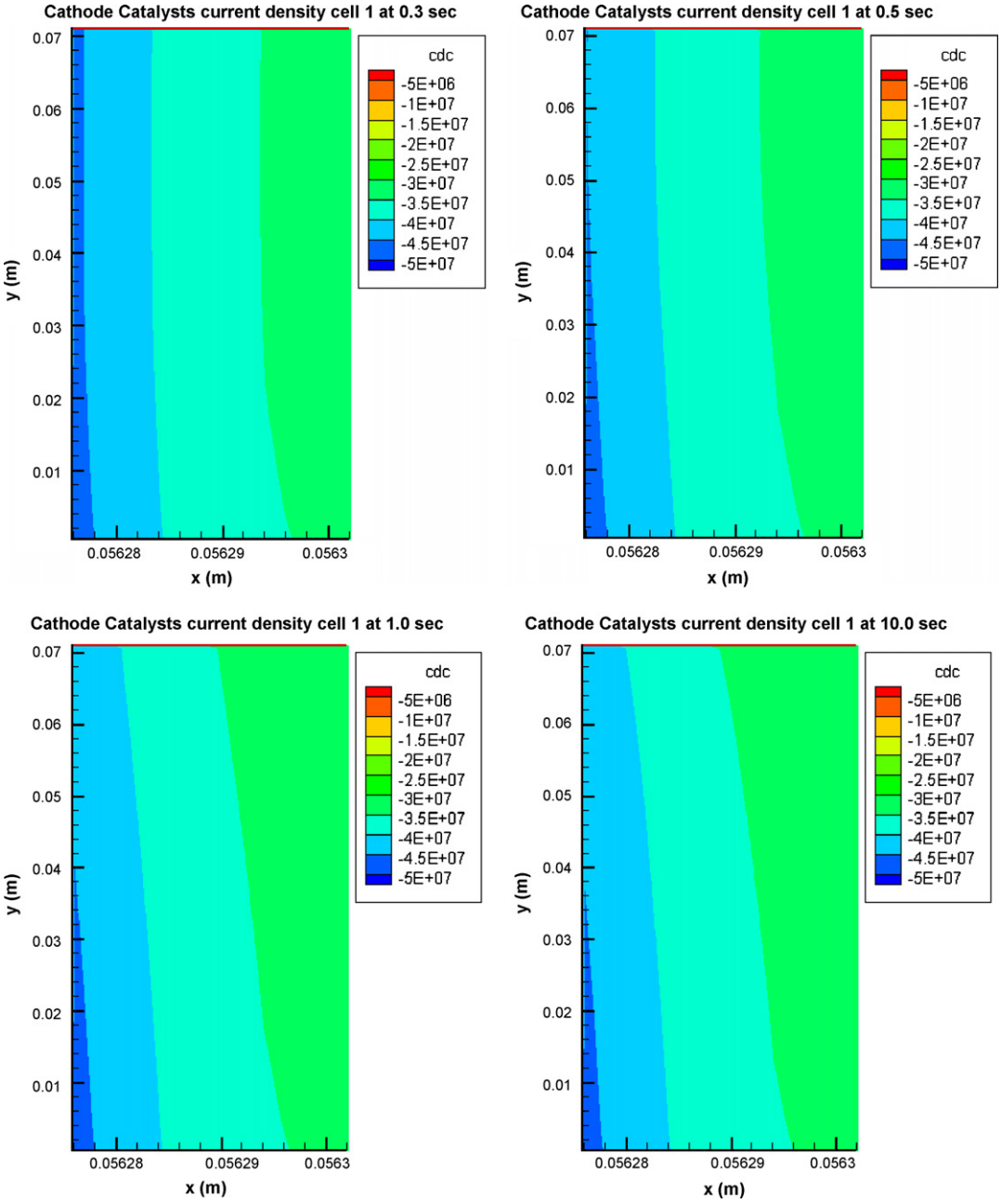


Fig. 6. Current density on the cathode side (Unit: A $m^{-3}$).

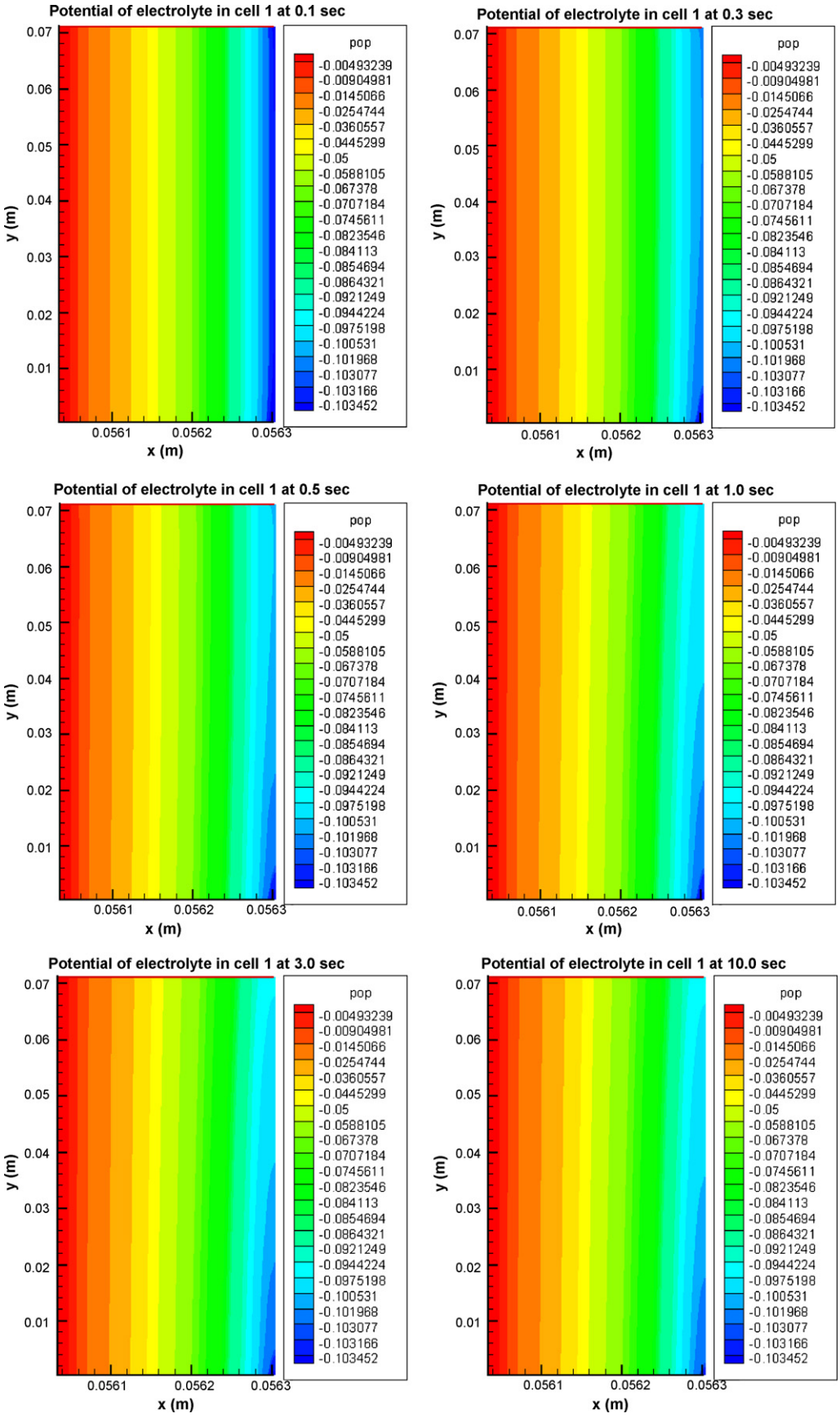


Fig. 7. Membrane potential dynamics at the cell 1 (Unit: V).

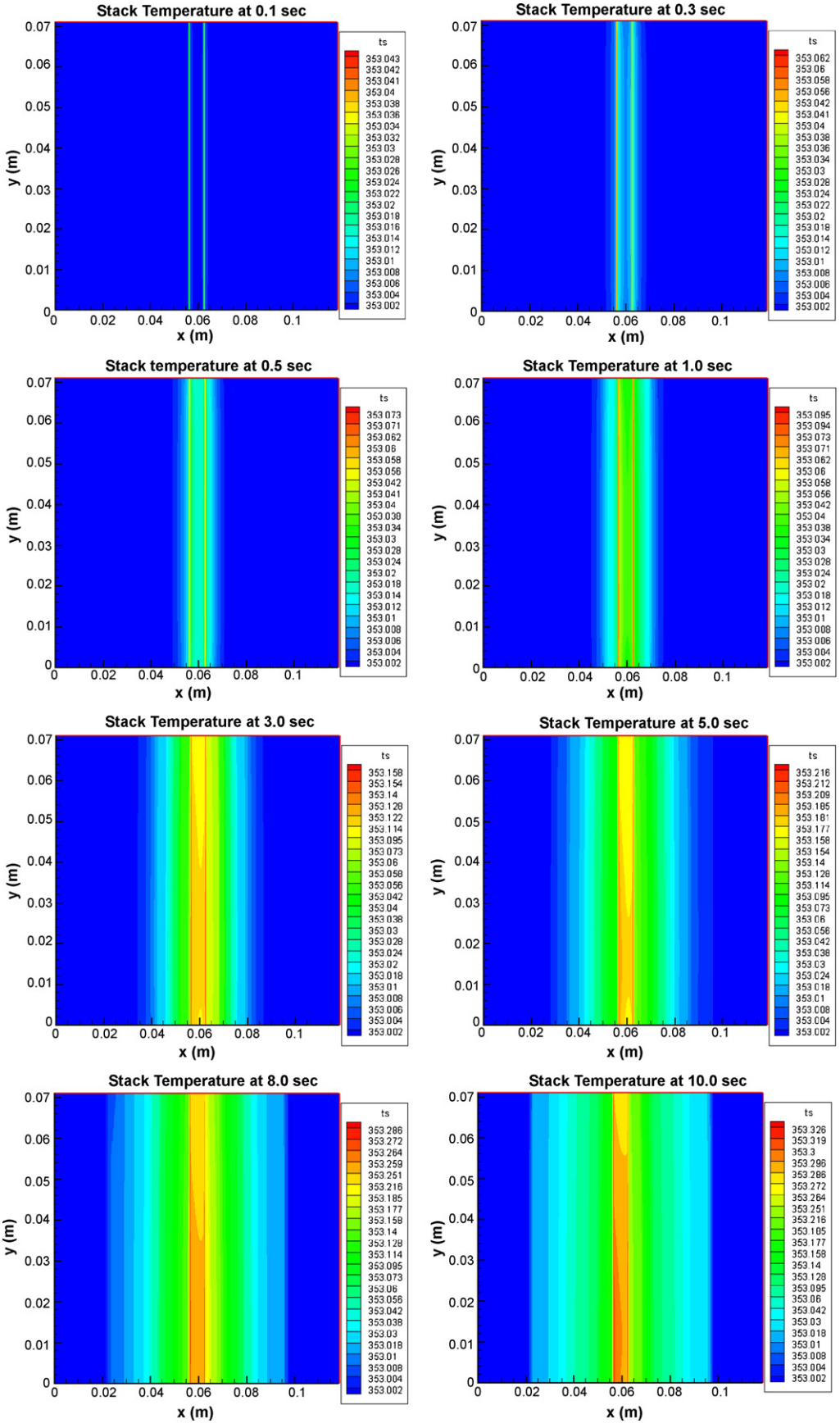


Fig. 8. Stack temperature 2D (Unit: K).

temperature in the first 10 s is not so high and the influence is negligible. The overpotential on the left side of the cathode catalyst in the cell 1 is higher than that on the right side because the protons flow in the direction where the electrolyte potential decreases.

The concentration of the reactant at the inlet side is higher than that on the outlet side. Therefore, the current density gets higher at the inlet side. However, the magnitude of the influences through and along the planes depends upon, which one is dominant in an operating condition. For an example, when the concentration of the reactants decreases along channel, the overpotential gets increased because of the change of the membrane conductivity that is explained in details by Ju et al. [12]. As a matter of fact, water generated is being accumulated at the outlet side and hydration rate in the membrane becomes higher, while the inlet side relatively gets dehydrated because of less water accumulated. Likewise, the concentration of the reactants gradually decreases through the planes from the GDL to the membrane, while the overpotential increases. As a consequence, the source term of the current density depends upon an instant which one is dominantly influenced.

It is observed that the current density along the channel direction is dynamically varying within the 1 s. The current density at the outlet side decreases, while the one at the inlet side increases. This effect is caused by the change of the concentration of the reactants along the channel.

The results presented in this paper are not able to represent some effects associated with water concentration, overpotentials, concentration of the reactants caused by two-phase flow. In addition, due to the limited calculation time of the codes developed, simulation has been run for only 10 s and the steady state is not reached yet.

Fig. 7 shows the simulated results of a phase potential field in the electrolyte of the cell 1 representing a catalyst and membrane. The potential field has reached to a steady state at the first second, where the potential drop in the membrane along the channel direction is not high. In fact, the gradient of the membrane conductivity along the gas channel direction is negligible because of the constraints on the single phase and requires a long computational time to see the effects. Conversely, the potential in the cathode catalysts shows a high gradient, because the chemical reaction at the inlet side is high than those on the outlet side. Subsequently, protons at the inlet side are more consumed and tend to flow toward the inlet direction.

When the reactant concentration is large, the source term of current density is bigger. As a result, the potential of the electrolyte at the inlet gets smaller, the over-potential gets smaller. It decreases the source term of the current density, finally an equilibrium state is reached.

Fig. 8 illustrates a transient behavior of the temperature distribution for a stack including two cells at eight different instants: 0.1, 0.3, 0.5, 1, 3, 5, 8, and 10 s. When the stack gets operated, the heat is generated and temperature rises.

At the first instant, the most heat is generated in two catalyst layers when the reaction begins and at the same time the entropy change occurs. Thus, the temperature peak appears in the cathode catalyst layers of two cells instead of the

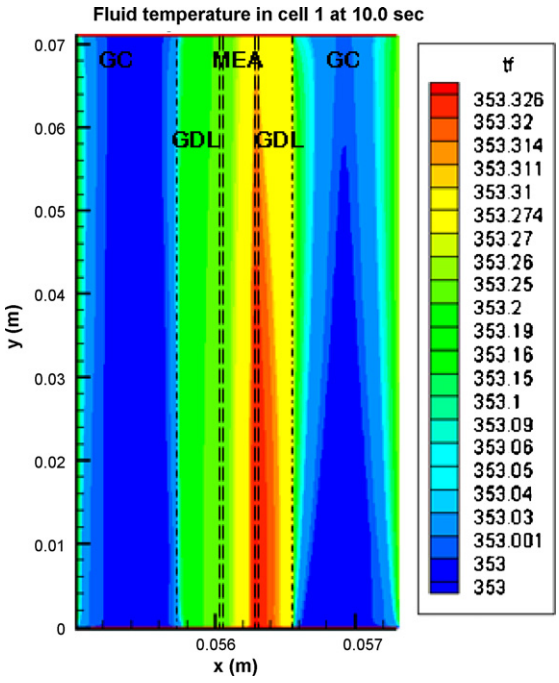


Fig. 9. Fluid temperature.

membrane layer. In addition, the source term of the current density at the inlet region is higher than that of the outlet region, so the temperature along the channel direction gets decreased.

At the following instants, the heat flux begins to diffuse and temperature in all the planes of the stack rises.

Fig. 9 shows the temperature distribution of the gases and fluids in the cell 1 that includes two gas flow channels. The geometry of the cell is referred to Tables 2 and 3. The temperature profiles in both of channels are not symmetrical and the temperature on the cathode side is higher than the anode side because of the larger amount of heat generated in the cathode than in the anode. Due to the large heat transfer area of the GDL by the porosity, the temperature gradient between the catalyst and the GDL is relatively low, while the temperature drop at the interface between the GDL and the flow channel is high.

Fig. 10 shows the dynamics of the temperature distribution. Firstly, the temperature dynamically changes at different instants when the times go by from 0.1, 0.3, 0.5, 1, 3, 5, 8, and 10 s. It is observed that the temperature in the cells at the very beginning rapidly rises from an initial value of 353 K because of the heat generated in the catalysts by chemical reaction and in the membranes by ohmic losses. The shapes of the rising temperature in both of cells are identical. It is shown that the peak value in the catalyst layer of the cell 1 gradually becomes higher than the one in the cell 2. In fact, the endplate assembly used for the stack should be comparably thick because of the mechanical requirement for robustness and represents two large heat sinks. However, the distance between the layer with the heat source and the end assemblies in the stack is different in a typical stack construction and consequently heat transfer properties are not identical to each other. Finally, the temperature profile through

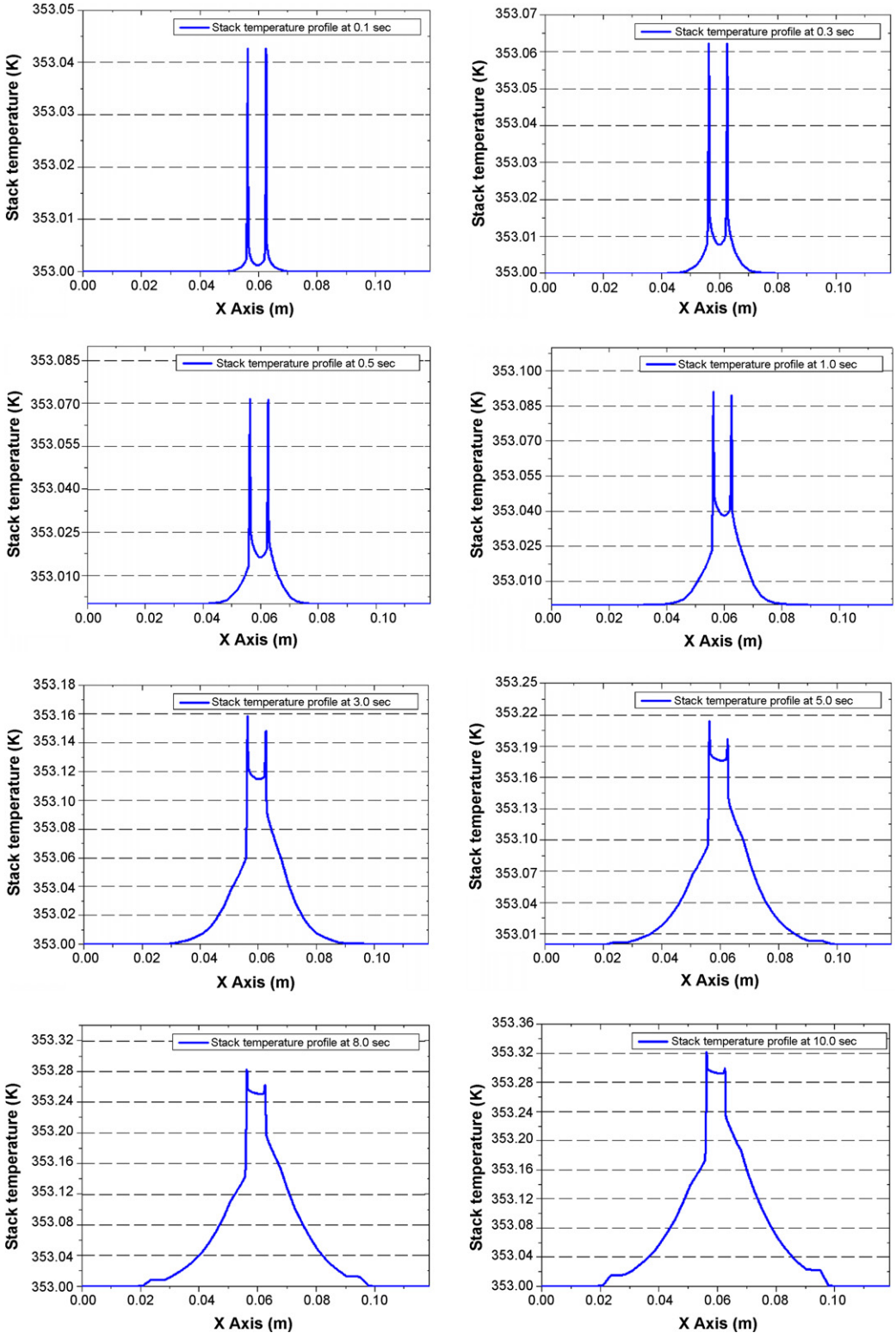


Fig. 10. Temperature distribution through the plane.

the plane gets asymmetrical and the one on the left side cell becomes higher.

Fig. 11 shows the temperature distribution in the cells 1 and 2, which allows for a direct comparison of how the temperature profiles are dynamically changing at a different instant. It is shown that the shapes of the temperature profile at the 0.1 s are the same. The endplate effect is to recognize at the 0.2 s, where the cell 1 shows a low temperature at the anode side. At the 0.5 and 1 s, the gap between two cells gets larger. The temperature of the cell 1 on the cathode side is lower than that of the cell 2,

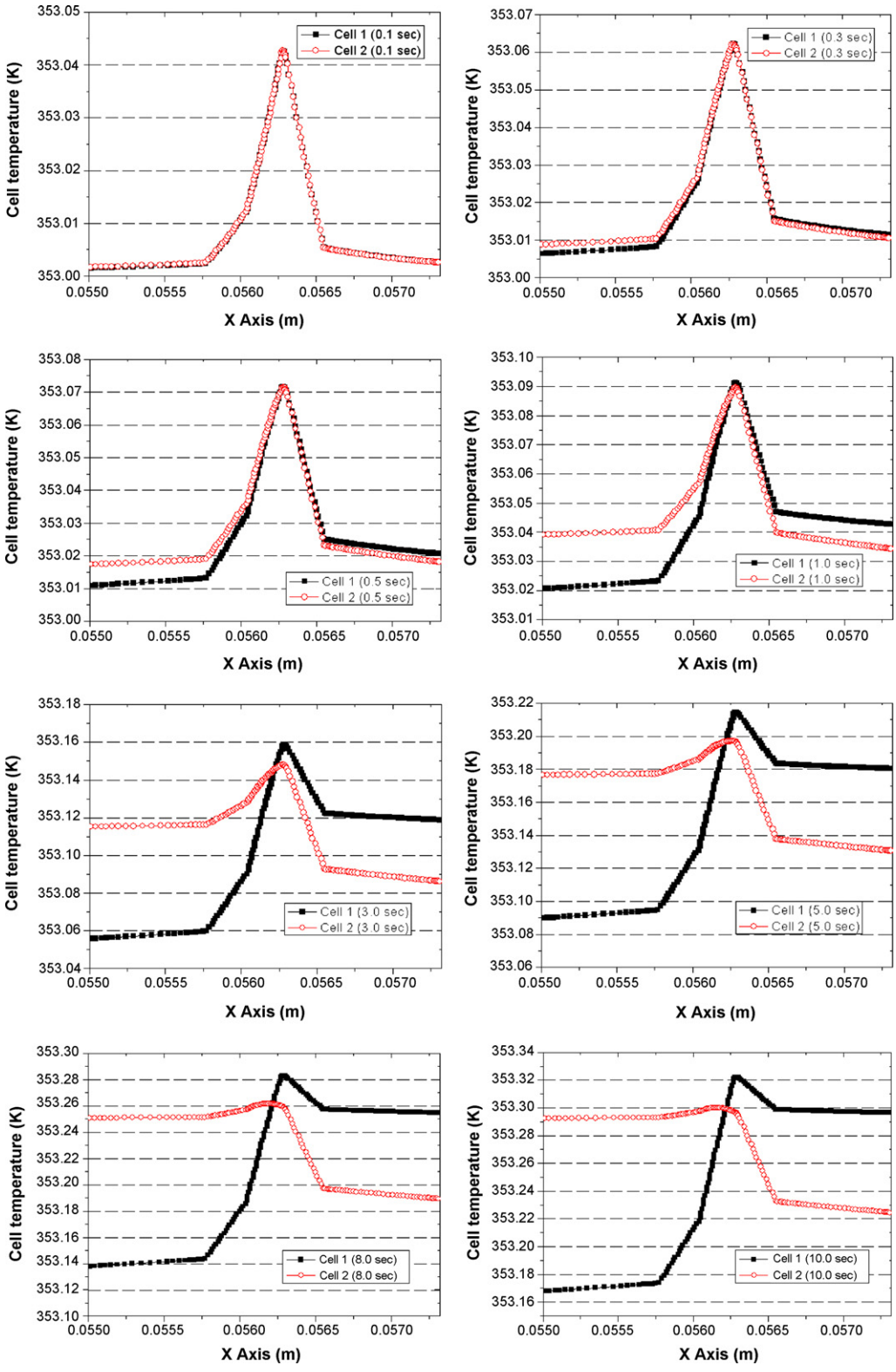


Fig. 11. Temperature distribution through the plane.

while the temperature of the cell 1 on the anode side is higher than the one of the cell 2.

At the 1 and 3 s, the gaps on the both sides get larger and the peak values of temperature for both cells begin to deviate. The temperature of the cell 1 becomes higher than the cell 2.

At the 8 and 10 s, the behavior of the temperature profiles remains as the same as before. As a consequence, the perfor-

mance of the cell 1 becomes better than the cell 2. However, there are some constraints on the analyses conveyed because of ignored effects of two-phase flow.

## 5. Conclusion

In this work, a new dynamic 2D model for the PEM fuel cell stack considering the fluid and thermal characteristics is proposed. Emphases are placed on numerically solving the equations and effects of the temperature distribution on the stack performance, which varies dynamically during operations. The model developed assumes a structure sandwiched by layers that include membrane, catalysts, gas diffusion layers, bipolar plates and endplate assembly. The domains specified for the modeling are determined by the way of physically working principles rather than the layers used commonly. The separate setup of modeling domains provided an easiest way to understand the physics involved and consequently reduce the development time for the codes.

The model can calculate dynamic distribution of pressure and reactants, current density, temperature and potentials in a stack. Due to the consideration of two adjoining cells, the models can be used for particularly designing a stack and BOPs along with controls, where the interacting influences from the neighboring cells plays a significant role. For example, calculations of temperature distribution across the stack can contribute to develop a thermal management strategy for the coolant circuit.

The analyses and modeling proposed lay a groundwork, which ultimately should increase efficiency and performance of the system. Future work will include an expansion of the model for two-phase flow in a 3D geometry and optimize the model with 1D and 2D.

## References

[1] M. Ceraolo, C. Miulli, A. Pozio, J. Power Sources 113 (1) (2003) 131–144.
[2] J.T. Pukrushpan, A. Stefanopoulou, H. Peng, Proceedings of the 2002 American Control Conference, 2002, pp. 3117–3122.
[3] S.D. Gurski, D.J. Nelson, Presented at the SAE 2003 World Congress & Exhibition, Detroit, MI, March, 2003.
[4] T. Nguyen, R. White, J. Electrochem. Soc. 140 (1993) 2178–2186.
[5] D. Natarajan, T.V. Nguyen, J. Power Sources 115 (2003) 66–80.
[6] D. Singh, D.M. Lu, N. Djilali, Int. J. Eng. Sci. 37 (1999) 431–452.
[7] V. Garua, H. Liu, S. Kakac, J. AIChE 44 (1998) 2410–2422.
[8] S. Um, C.Y. Wang, K.S. Chen, J. Electrochem. Soc. 147 (2000) 4485–4493.
[9] S. Dutta, S. Shimpalee, J.W. Van Zee, Int. J. Heat Mass Transfer 44 (2001) 2029–2042.
[10] S. Um, C.Y. Wang, J. Power Sources 125 (2004) 40–51.
[11] Y. Wang, C.Y. Wang, J. Power Sources 147 (2005) 148–161.
[12] H. Ju, H. Meng, C.Y. Wang, Int. J. Heat Mass Transfer 48 (2005) 1301–1315.
[13] M. Sundaresan, R.M. Moore, J. Power Sources 145 (2) (2005) 534–545.
[14] M. Sundaresan, PhD Dissertation, University of California at Davis, 2004.
[15] M. Wohr, K. Bolwin, W. Schnurnberger, M. Fischer, W. Neubrand, G. Eigenberger, Int. J. Hydrogen Energy 23 (3) (1998) 213–218.
[16] M. Lampinen, M. Fomino, J. Electrochem. Soc. 140 (12) (1993) 3537–3546.
[17] B. Wetton, K. Promislow, A. Caglar, Second International Conference on Fuel Cell Science, Engineering and Technology, 2004.
[18] P. Berg, K. Promislow, J. St-Pierre, J. Stumper, B. Wetton, J. Electrochem. Soc. 151 (2004) A341–A353.
[19] Y. Shan, S.Y. Choe, J. Power Sources 145 (1) (2005) 30–39.
[20] Y. Shan, S.Y. Choe, J. Power Sources 158 (1) (2006) 274–286.
[21] S.V. Patankar, Numerical Heat Transfer and Fluid Flow, Hemisphere, New York, 1980.
[22] S.M. Senn, D. Poulikakos, J. Power Sources 130 (2004) 178–191.
[23] T.E. Springer, T.A. Zawodzinski, S. Gottesfeld, J. Electrochem. Soc. 138 (1991) 2334–2341.
[24] B.M. Eaton, The Virginia Polytechnic and State University, Master Thesis, 2001.
[25] P. Berg, K. Promislow, Nanotechnology 3 (2003) 493–496.
[26] Y. Wang, C.Y. Wang, J. Electrochem. Soc. 152 (2005) A445–A453.